Title

Mechanical reliability and durability of SOFC stacks. Part II: Modelling of mechanical failures during ageing and cycling

Journal

International Journal of Hydrogen Energy, 37(11)

ISSN

0360-3199

Authors

Nakajo, Arata
Mueller, Fabian
Brouwer, Jacob
et al.

Publication Date

2012-06-01

DOI

10.1016/j.ijhydene.2012.03.023

INTERNATIONAL JOURNAL OF HYDROGEN ENERGY 37 (2012) 9269–9286

Available online at www.sciencedirect.com

SciVerse ScienceDirect

journal homepage: www.elsevier.com/locate/he

Mechanical reliability and durability of SOFC stacks. Part II: Modelling of mechanical failures during ageing and cycling

Arata Nakajo [a,*], *Fabian Mueller* [b], *Jacob Brouwer* [b], *Jan Van herle* [a], *Daniel Favrat* [a]

[a] *Laboratoire d'Energétique Industrielle (LENI), Institut de Génie Mécanique, Ecole Polytechnique Fédérale de Lausanne, 1015 Lausanne, Switzerland*

[b] *National Fuel Cell Research Center, University of California, Irvine, CA, United States*

ARTICLE INFO

Article history:
Received 29 August 2011
Received in revised form
29 February 2012
Accepted 7 March 2012
Available online 13 April 2012

Keywords:
Solid oxide fuel cell
Thermal stresses
Degradation
Creep
Contact analysis

ABSTRACT

Intricate relationships between mechanical and electrochemical degradation aspects likely affect the durability of solid oxide fuel cell stacks. This study presents a modelling framework that combines thermo-electrochemical models including degradation and a contact thermo-mechanical model that considers rate-independent plasticity and creep of the components materials and the shrinkage of the nickel-based anode during thermal cycling. This Part II investigates separately or together the contributions of mechanical and electrochemical degradation on the behaviour during long-term operation and thermal cycling.

Electrochemical degradation modifies the temperature profile under constant system power conditions and consequently the risks of cell failure. Irreversible deformation of the stack components causes losses of contact pressure during thermal cycling and variation of the electrical load and changes the risks of anode and cathode cracking. Critical tensile stress progressively develops in the cell compatibility layer (GDC between YSZ and LSCF) during thermal cycling depending on the temperature profile in operation.

1. Introduction

The end of operation of a solid oxide fuel cell (SOFC) stack ultimately occurs due to the loss of structural integrity of one or several of the cells, as highlighted by several short-stack experiments, e.g [1–4]. We believe this is the result of the accumulation during operation, of physico-chemical alterations inducing a weakening of the materials and interfaces, of plastic and creep deformations, and of the modification of the temperature profile, due to the degradation of the electrochemical performance of the cells. Mechanical issues do not, however, exclusively occur after prolonged use. Inappropriate control during start-up and shut-down and/or following of the electrical power demand, harsh characterisation procedures and thermal cycling can induce discrete failures [5,6].

Despite the evidence of mechanical issues in SOFCs, which are experienced even during laboratory button cell tests, this topic is still receiving limited attention. Efforts are seen as standalone tasks, owing to the different experimental and modelling techniques that are required to gather the essential information, whereas mechanical failures in SOFCs are likely intricately related to chemical and electrochemical aspects.

The central component in a stack is the membrane electrode assembly (MEA). As for any multilayered system made of brittle materials, the MEA is prone to failures related to residual

* *Corresponding author*. Tel.: +41 21 693 35 05.
E-mail address: arata.nakajo@epfl.ch (A. Nakajo).

0360-3199/$ – see front matter Copyright © 2012, Hydrogen Energy Publications, LLC. Published by Elsevier Ltd. All rights reserved.
doi:10.1016/j.ijhydene.2012.03.023

Nomenclature

Latin letters

$\mathcal{V}_r$	reference volume, m^3
E	Young modulus, Pa
E_a	activation energy, J mol^{-1}
h	thickness, m
j	current density, A m^{-2}
k_o	kinetic constant
m	Weibull modulus
m^{crp}	stress exponent
n	porosity
T	temperature, K
U	electric potential, V

Greek letters

ε	strain
ν	Poisson coefficient
σ_Y	elastic limit, Pa

Indices

THC	thermal cycle
o	initial, unperturbed or characteristic
red	reduction

Superscripts

crp	creep
p	plastic

Acronyms

ASR	area specific resistance
Cou	counter-flow
Co	co-flow
CTE	coefficient of thermal expansion
FU	fuel utilisation
GDC	gadolinia-doped ceria
GDL	gas diffusion layer
GLS	glass-ceramic sealant
GSKT	compressive gasket tied at the sealing interfaces
GSK	compressive sealing gasket
IV	current-voltage characterisation
LSCF	lanthanum strontium cobaltite ferrite
LSM	lanthanum strontium manganite
MEA	membrane electrode assembly
MIC	metallic interconnect
PR	methane conversion fraction in the reformer
RT	room temperature
SRU	standard repeating unit
THC	thermal cycle to room temperature
TPBL	triple phase boundary length
TPB	triple phase boundary
YDC	yttria-doped ceria
YSZ	yttria-stabilised zirconia

stresses generated during the manufacturing process, and to further thermal cycling and prolonged exposure to aggressive environments. During operation, physico-chemical alterations in the bulk and at the interfaces between the materials, ensuing sole or combined effects of material incompatibilities [7,8], particle growth [9–13] and contamination [14] have a consequence on the long-term reliability and resistance towards transient operation and thermal and reoxidation cycling [15–18]. Mori et al. [19] and Sun et al. [20] report a shrinkage of the Ni-yttria stabilised zirconia (YSZ) anode during thermal cycling. Discrete element modelling [21] is a means to clarify the mechanisms. Anandakumar et al. [22] have investigated the beneficial use of graded materials on the risk of cell failure. The stress state in the different layers is not permanent, due to the temperature-dependent coefficients of thermal expansion (CTE) and creep [23].

The rationale behind the development of anode-supported cells and reactive cathode materials, such as lanthanum strontium cobaltite ferrite (LSCF) or composite lanthanum strontium manganite (LSM)-YSZ is the reduction of the operating temperature, which enables a wider choice in the interconnecting, sealing and gas diffusion layer (GDL) materials, with beneficial cost implications. The mechanical behaviour at high temperature of these components typically made of metallic alloys, glass-ceramics, mica or vermicullite, is complex. The available data cannot support the development of detailed constitutive relations that are needed for a reliable description [24,25]. The loss of integrity of the stack components is tackled by dedicated modelling. Similar to the MEA, a metallic interconnect (MIC) is a multilayer of finite durability [26], wherein, in state-of-the-art solutions, a ceramic coating slows the growth of the oxide scale of lower electrical conductivity and the vaporisation of chromium, that poisons the cathode. Fracture mechanics approaches have been applied to study the cracking of the glass-ceramic or sealing interfaces, commonly observed during thermal cycling [27,28].

The aforementioned component failures indirectly affect the integrity of the cells, by modifying the electrochemical performance [29] and by causing localised reoxidation or reduction of the anode and cathode, respectively [2], the sole mechanical interactions between the components can also promote cell cracking. The choice of GDL and sealing solutions determines the mechanical interactions between the components. The difficulty to ensure reproducible mechanical properties of the sealants and GDL materials [30,31] can potentially cause uneven gas supply among the stacked single repeating units (SRU), alter the electrical contact and relieve the needed contact pressure on compressive gaskets. Additional stress and uneven plastic and creep deformation arise from the non-uniform distributions of temperature and gas composition over a SRU in operation.

In a SOFC stack, the flatness of the SRUs is not enforced. Even though a conservative thickness of the MIC is selected to prevent thermal buckling [32], the slight curvature of the cells and the asymmetry, due to the different materials for use in reducing and oxidising atmosphere [33], cause a slight bending of the SRUs located far from the ends or stabilising plates. This SRU deflection evolves as operation proceeds, driven by irreversible deformations that relieve stress at high

temperature in steady conditions, but results in another source of history-dependent stress.

Modelling studies at the stack level that include time, at the scale of the degradation processes, remain few [34,35]. The studies by Lin et al. [36] and Liu et al. [37] investigate ageing from a structural perspective. The former have included creep in their model to simulate the effects of the change of curvature of a SRU on the geometry of the gas channels, hence possible subsequent gas distribution problems, whereas the latter have focused on MIC coating durability. Otherwise, studies of long-term issues are restricted to cycling or transient operation, with an emphasis on either the sealing system [38–40], MEA alone or plastic deformation [26,32,41,42].

The present study comprises two parts that enlarge with structural analysis our investigations on the degradation of the stack electrical performance [43–45]. Part I [46] focuses on the influence of the SOFC stack operation parameters on the mechanical reliability, whereas this Part II investigates the combined or separate effects of electrochemical and mechanical degradation on the structural reliability of a planar stack with anode-supported cell. The analysis encompasses rate-independent plasticity and creep deformation of the components and shrinkage of the anode material, together with electrochemical degradation to gain knowledge on the detrimental phenomena acting during combined steady-state operation, performance characterisation and thermal cycling, under practical operating conditions. The framework is a set of existing models. The stresses in the components of a SRU are computed from the temperature profiles generated by a thermo-electrochemical model, that includes degradation phenomena [43,44,47,48]. Operating conditions optimised for the highest system electrical efficiency at start or at long-term operation form the basis of the analysis [43,44]. The capabilities of a structural model of a SRU based on anode-supported cells, which considers the interaction between the components and the curvature of the cell [32,42] are extended for the simulation of the effects of creep during prolonged operation and of the shrinkage of the Ni-YSZ anode. Stacking is modelled by modified periodic boundary conditions. The mechanical properties of the materials are extracted from the compilation provided in Refs. [24,25].

2. Modelling approach

Part I [46] summarises the modelling approach, which consists in coupling a set of thermo-electrochemical and structural models, implemented in gPROMS [49], an equation-oriented process-modelling tool and ABAQUS [50], a numerical tool based on the finite-element method. The analysis focuses on the planar, intermediate-temperature stack based on anode-supported cells with an active area of 200 cm^2, developed at LENI-EPFL within the European FP6 FlameSOFC project [24,51]. Fig. 1 depicts the SRU geometry. Boundary conditions in both types of models are imposed to simulate a SRU in a stack [42,46]. This section focuses on the additional features needed for the analysis of electrochemical and thermo-electrochemical degradation.

2.1. *Thermo-electrochemical model*

In contrast to Part I [46], degradation effects of the temperature profile are investigated here (see Section 3). The degradation phenomena implemented in the electrochemical model are the (i) decrease of ionic conductivity of 8YSZ, (ii) MIC corrosion, (iii) anode nickel particle growth (iv) chromium contamination and (v) formation of zirconate in LSM-YSZ cathode. Refs. [43,44,47] describe in details the modelling approach and the calibration with data from two segmented-cell experiments [52,53]. The main features are:

- A classical percolation model predicts the reduction of the triple phase boundary length (TPBL) due to the growth of the nickel particles in the anode. The semi-empirical relation for the evolution of the nickel particle radius depends upon temperature, steam and hydrogen partial pressure and tends to a maximum value due to the mechanical constraint imposed by the YSZ network. The time to reach the final state in the model spans from 1000 h to 10000 h under the local conditions found in an intermediate-temperature SOFC stack running on partially or fully pre-reformed methane with a steam-to-carbon ratio of 2 [47]. Comparison between a simple interfacial model for the hydrogen oxidation (HO) and a distributed charge-transfer model has validated the use of the former.
- An empirical model reproduces the experimental data on the decrease of the ionic conductivity of 8YSZ samples during ageing in air. It is unclear from the available experimental data, whether the degradation proceeds monotonically or reaches a plateau. The final value in the model for a given temperature is reached after 500 h–2500 h [47]. This degradation process affects both the electrolyte and the 8YSZ phase in the LSM-YSZ cathode. Recovery of the ionic conductivity is not allowed.
- The maximum SRU temperature in intermediate-temperature SOFC is set, among other reasons, by the oxidation resistance of the metallic components. A consistent set of data on the temperature dependence of the evolution of the area specific resistance (ASR) of coated MIC could not be found. The relation by Liu et al. [26] for the growth of the oxide scale under a $Mn_{1.5}Co_{1.5}O_4$ coating that is used in the present study is valid at 1073 K only.
- The modelling of chromium contamination of a LSM-YSZ cathode assumes the progressive blocking of the active sites by the electrochemical deposition of Cr_2O_3, which is described by a Butler–Volmer relation. The deposition rate depends upon the steam and $CrO_2(OH)_{2(g)}$ partial pressures and the local overpotential within the composite cathode. Many other Cr volatile species can be involved in a SOFC stack [54–57]. For consistency, a small amount of steam is needed in the air. The value of 0.1% used here is typical for compressed air, commonly used in stack testing [8]. It should be emphasised that for higher humidity, other phenomena, not necessarily related to chromium contamination, may predominantly cause the degradation of the LSM-YSZ cathode [58].
- An indicator provides the start of formation of undesirable zirconate phases in the LSM-YSZ cathode. The thermodynamic data on the critical oxygen partial pressure from Liu

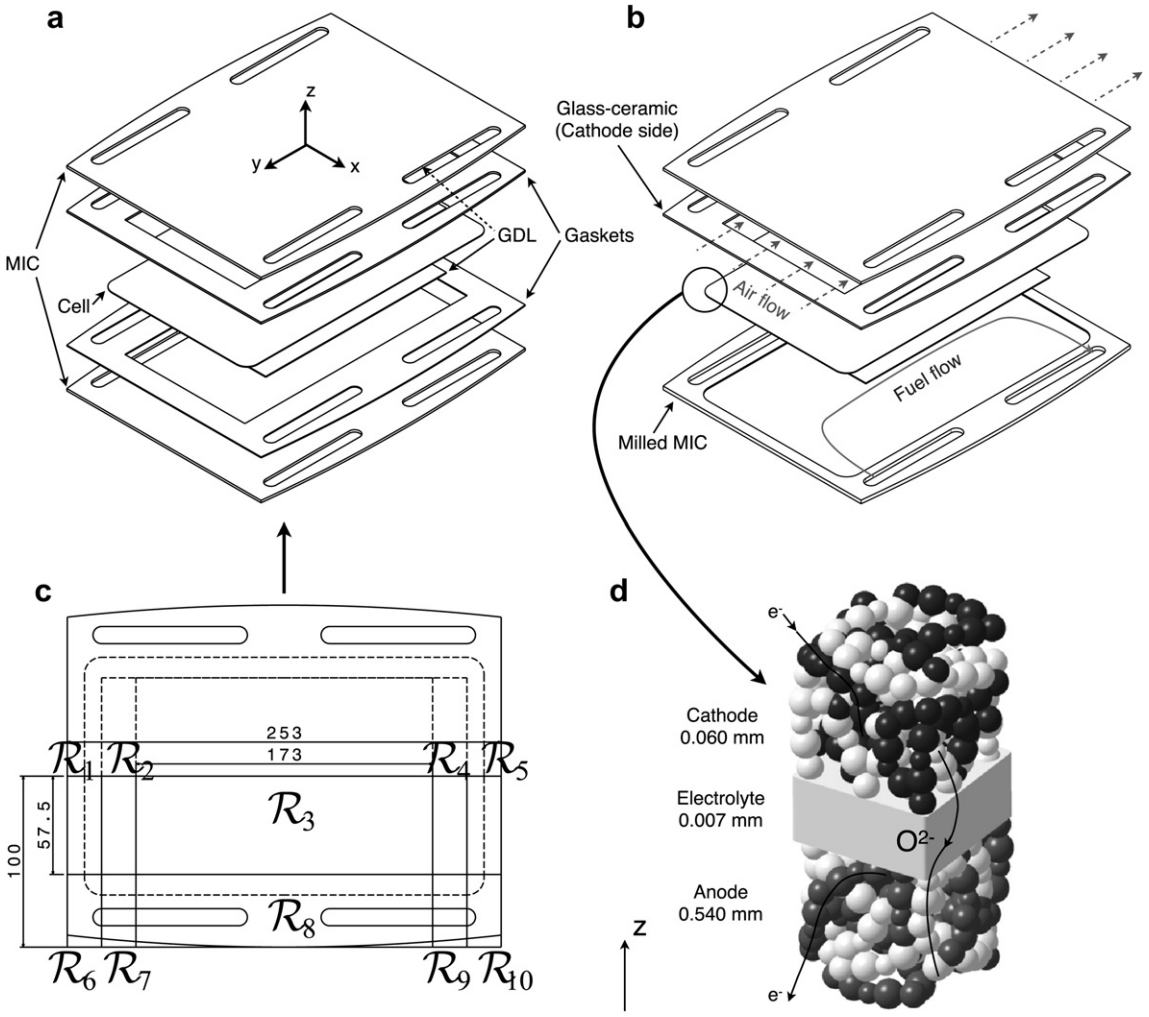

Fig. 1 – View of the FlameSOFC SRU design with (a) compressive gaskets and (b) glass-ceramic sealants. (c) indicates the computation do- mains in the 2D SRU thermo-electrochemical model. (d) provide a schematic view of the MEA in the electrochemical model, for the case of a cell with LSM-YSZ cathode.

et al. [7] is interpolated and compared with the local one, computed from the local overpotential and oxygen gas-phase concentration. The detrimental impact on the oxygen reduction reaction is not included.

2.2. *Structural model*

Considered long-term mechanical degradation phenomena are (i) creep in the metallic components and cell layers, (ii) shrinkage of the Ni-YSZ anode, when subjected to thermal cycling and (iii) alteration of the strength of Ni-YSZ during ageing. Creep and rate-independent plasticity are uncoupled [24,50] and the analysis is restricted to secondary creep. The time-dependence of the creep deformation of ferritic alloys for SOFC application reported during tests under constant stress and temperature [59] are for instance not considered. The ferroelastic behaviour [60] reported for LSCF [61] is not implemented. These simplifications are believed acceptable for the present study and will be the subject of future model improvements. The shrinkage of the anode is assumed uniform, because conditions-dependent data could not be found [19,20]. Shrinkage is implemented after a thermal cycle to room temperature, using the swelling feature of ABAQUS [50].

The whole set of time- and conditions-dependent mechanical material properties, when available from literature, is extracted from the compilation in Refs. [24,25]. Table 1 provides the range of the values used in the present study. XRD measurements of the stress in the electrolyte of anode/electrolyte bilayers from the literature have been used to validate the calculated residual stresses in the cell layers as a function of temperature before and after reduction [23].

3. Investigated cases

Cases differing in terms of design alternatives and of implemented physics were selected to investigate the separate or combined effect of electrochemical and mechanical degradation. Design alternatives treated in this study differ in the choice of:

Table 1 – Overview of the mechanical properties of the constituents of the SRU, from the data compilation in [24,25].

	T (K)	n (%)	h (m)	ε_{red} (%)	ε_o^p (–)	ε_{THC} (–)	E[c] (GPa)	ν	CTE$\times10^{-6}$ (K^{-1})[c]	k_0^{crp} ($MPa^m h^{-1}$)	E_a^{crp} (kJ mol^{-1})	m^{crp}	σ_y (MPa)	σ_0 (MPa)	m	$\mathcal{V}_r$ (mm^3)
Cathode	RT	29–30[c]	60e-6	–	0 (C1)	–	41.3	0.28	12.16	5.551e10[i]	392[i]	1.7[i]	–	52	6.7	1.217
(LSM)	1073			–		–	48.3	0.28					–	75	3.7	2.836
Cathode	RT	29–30[c]	60e-6	–	−1.25e−7(C2)	–	10[d]	0.32	15.34	5.551e10	392	1.7	–	134[k]	3.8[k]	1.028[k]
(LSCF)	1073			–		–							–	183[k]	5.7[k]	0.575[k]
Electrolyte	RT	0	7e-6	–	−3.16e−4(C1)	–	196.3	0.32	10.21	1.836e07	640	0.5	–	232	5.7	0.535
(YSZ)	1073			–	−3.15e−4(C2)	–	148.6	0.32					–	154	8.6	0.301
Anode	RT	19[d]	542e-6	−0.01	0 (C1)	−2.2e−6	124.9	0.39	12.37	–	–	–	–	–	–	–
(NiO-YSZ)	1073			–		–	119.9	0.39					–	–	–	–
Anode	RT	38–40	542e-6	–	–	–	72.5	0.39	12.41	1.040e20	640	2.5	–	79 (73,85)	7 (5,10)	4.812
(Ni-YSZ)	1073			–	–	–	58.1	0.39					–	–	–	–
compat. layer	RT	0	4e-6[l]	–	−2.61e−5(C2)	–	196.3[e]	0.32	12.63	6.768e04	264	1.0	–	134	3.8	1.028
(GDC)	1073			–		–	148.6[e]	0.32					–	183	5.7	0.575
GDL anode[h]	RT	93	1e-3	–	–	–	0.37	0.3	16.20	7.17e10	284	4.6	0.9	–	–	–
(Ni)	RT	95		–	–	–	0.09	0.3					0.31	–	–	–
	1073	93		–	–	–	0.25	0.3	16.20				0.26	–	–	–
	1073	95		–	–	–	0.06	0.3					0.09	–	–	–
GDL cathode[h,j]	RT	93	2e-3	–	–	–	0.15	0.3	11.80	3.38e13	343.9	4.73	1.27	–	–	–
(Haynes230)[a]	RT	95		–	–	–	0.09	0.3					0.92	–	–	–
	1073	93		–	–	–	0.12	0.3	11.80				0.88	–	–	–
	1073	95		–	–	–	0.07	0.3					0.63	–	–	–
MIC	RT	0	1.25-2e-3	–	–	–	216.0	0.3	11.80	1.222e06	343.9	4.73	248	–	–	–
(Crofer22APU)[a]	1073			–	–	–	65.9	0.3					35	–	–	–
Gasket	RT	na	1-2e-3	–	–	–	0.019[f]	0	10–13.9	–	–	–	–	–	–	–
(Flexitallic 866)[a]	1073			–	–	–							–	–	–	–
Glass-ceramic	RT	0	2e-3	–	–	–	67.4[g]	0.28	11.10	1.627e10	282.9	1.59	43–83	–	–	–
(G18)[b]	1073			–	–	–	14.4[g]	0.28					31–64	–	–	–

a Commercial denominations [70,71].
b BCAS glass [30].
c Values from RT to 1073 K. Temperature-dependent values implemented in the model.
d Assumed value [23].
e Values for YSZ.
f Through the thickness: full non-linear pressure–closure relation.
g From stress-strain curves, instead of impulse excitation technique [30]. Arbitrary value of 0.2 GPa before sealing procedure.
h Computed from dense values.
i Values for LSCF.
j CTE of Crofer22APU implemented.
k Values for dense GDC.
l 7 μm in thermo-electrochemical calculations.

- Anode-supported cell: differences in failure modes can be expected upon the choice of a cathode material. LSCF has a significantly higher CTE than LSM-YSZ and further requires a compatibility layer made of GDC, which has different mechanical properties than YSZ (see Table 1). Therefore, standard Ni-YSZ/YSZ/LSM-YSZ (C1) and LSCF cathode-based cell Ni-YSZ/YSZ/GDC/LSCF (C2) are investigated. Table 1 lists the thicknesses.
- Sealing solution: the choice of a sealing modifies the mechanical interactions between the components in a stack. The present study considers compressive gaskets (GSK), compressive gaskets tied at the sealing interfaces (GSKT) or glass-ceramic sealant (GLS). Compressive gaskets are 5% thicker than the GDLs to prevent the complete relief of contact pressure at specific location [42]. The assembly load applied in the simulations is 0.11 MPa (GSK) and 0.022 MPa (GLS) on the basis of the SRU footprint area.

The investigation of the effects of electrochemical and thermo-mechanical degradation on mechanical failure is based on four main cases:

- Case 1 (C1, GSK): the separate effects of the evolution of the temperature profile induced by the degradation of the electrochemical performance are investigated.
- Case 2 (C1, GSK or GLS): the separate effects of creep in the metallic parts and glass-ceramic sealants are studied. Therefore, the temperature profiles are not affected by electrochemical degradation.
- Case 3 (C2, GSK): a previous study has shown that the gadolinia (GDC) or yttria-doped ceria (YDC) compatibility layer needed in an anode-supported cell with LSCF cathode may be vulnerable to combined ageing and thermal cycling [23]. Therefore, creep in the metallic components and C2 cell layers, except the LSCF cathode, is enabled, whereas degradation is disabled in the thermo-electrochemical calculations, since the mixed-ionic and electronic conductor (MIEC) model for the LSCF cathode does not include degradation processes. The irreversible and non-uniform deformation accumulated in the MEA layers complicates the submodelling procedure. This would require an in-depth modification of the MATLAB [62] routines that handle the restart and submodelling procedures. Therefore, the Weibull analysis and calculation of the stress in the cathode is not performed in this Case 3.
- Case 4 (C1, GSK): creep in the cell layers, except the cathode, and the shrinkage of the anode material when subjected to thermal cycles are added, and electrochemical degradation is enabled. For the same reason as for Case 3, the Weibull analysis and calculation of the stress in the cathode is not performed.

Thermo-electrochemical degradation simulations performed in Ref. [44] form the basis of the analysis. Fig. 2 depicts the simulation sequence applied for all cases after the initialisation (see Part I [46]) and repeated four times. The simulation sequence consists of thermal cycling (A in Fig. 2) to room temperature (RT), followed by current-voltage (IV) characterisation with inlet gas temperatures of 973 K, up to a fuel utilisation (FU) of 90% (B in Fig. 2) and operation in constant system specific electrical power output mode (C in Fig. 2). The ageing time depends upon the expected time scale of the investigated phenomena.

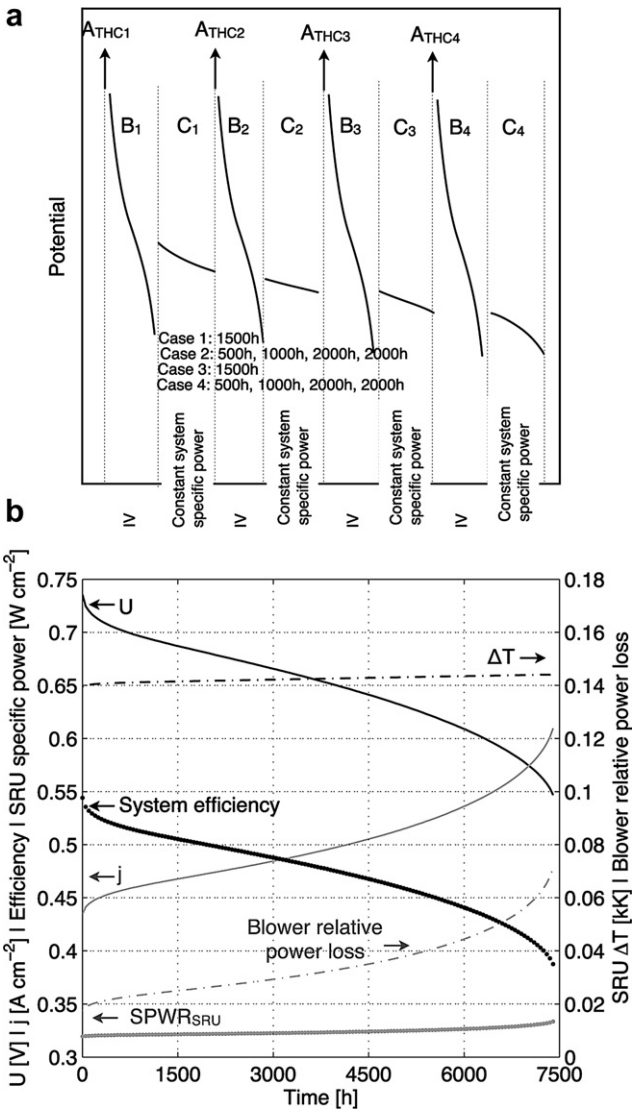

Fig. 2 – (a) Schematic view of the investigated sequences. (b) Typical evolution during operation at constant system power, of the system efficiency, SRU potential (left), current density (left), SRU specific power (left), temperature difference over the SRU (right) and relative blower power consumption as a fraction of stack power (right). Counter-flow, maximum SRU temperature of 1125 K, PR = 0.25 and system specific power of 0.29 W cm^{-2}.

In Case 4, the effect of the modification of the anode mechanical behaviour upon multiple thermal cycles [19] is simulated in an averaged manner. From the second thermal cycling step, an irreversible shrinkage strain of 2.2×10^{-4} is enforced in the anode at room temperature before proceeding further in the analysis, to simulate the effect of the modification of the anode mechanical behaviour upon thermal cycling [19]. This shrinkage strain corresponds to 50 cycles

Table 2 – Overview of the main operating conditions for the thermo-electrochemical simulations, from [43,44]. Ranges refer to values after 0 h and after 4500 h of operation at constant system specific power.

	PR	System specific power (W cm^{-2})	Cell	U (V)	j (A cm^{-2})	FU[a]	Air ratio	$T_{air\ inlet}$ (K)[a]
Co	0.99	0.29	C1	0.71–0.62	0.45–0.53	0.86	9.3–10.6	985
			C2[b]	0.75	0.44	0.90	7.87	964
Cou	0.25	0.29	C1	0.73–0.64	0.44–0.50	0.84	6.5–7.9	975
			C2[b]	0.74	0.44	0.90	6.39	963
Cou	0.99	0.29	C1	0.73–0.65	0.45–0.51	0.84	9.9–11.1	987
			C2[b]	0.76	0.44	0.89	9.83	983

a Constant during long-term operation.
b Degradation disabled in the electrochemical model.

[19], which is selected to represent harsh stack operating conditions (during stack lifetime, a total of 150 thermal cycles to room temperature is expected). In the case of glass-ceramic sealant (Case 2), the discrete material properties changes that are applied during the initialisation sequence do not completely reflect the continuous modification of the sealant properties that occurs during the sealing procedure. The stack is therefore annealed at a uniform temperature of 1073 K for 10 h, before the temperature profile of operation is applied. This time is referred to as 0 h.

Perfect control of the SOFC system enforces during degradation simulations (C in Fig. 2) (i) a system specific power of 0.29 W cm^{-2}, computed on the basis of the SRU active area of 200 cm^2, and (ii) a constant maximum SRU temperature of 1125 K. Previous analyses have demonstrated that a SOFC system for combined heat and power generation can have a large system operating envelope with sufficient heat integration for air preheating and fuel processing [63]. Therefore, the fuel utilisation, air inlet temperature, methane conversion fraction in the reformer (PR) and cathode and anode gas compositions are kept constant. Their optimal values in the view of highest system electrical efficiency at start (Case 3) and at long-term operation (Cases 1,2,4) have been determined in Ref. [43]. This study shows that electrochemical degradation scales with system specific power. The value of 0.29 W cm^{-2} represents harsh conditions and induces short lifetimes. Fig. 2b depicts the evolution of (i) the cell potential and averaged current density to meet the power demand and (ii) air ratio for stack thermal management. Table 2 lists the values of the SRU potential, current density, fuel utilisation, air ratio and air inlet temperature.

Temperature profiles computed by gPROMS are imported discretely in ABAQUS. Only simulation results where electrochemical degradation and creep proceed together (Case 4) could be affected by the update in time of the temperature profile in ABAQUS. In the conditions treated here, i.e., constant system power and fixed maximum SRU solid temperature for the electrochemical degradation simulations, tests showed that an update in time of 250 h provides sufficient accuracy.

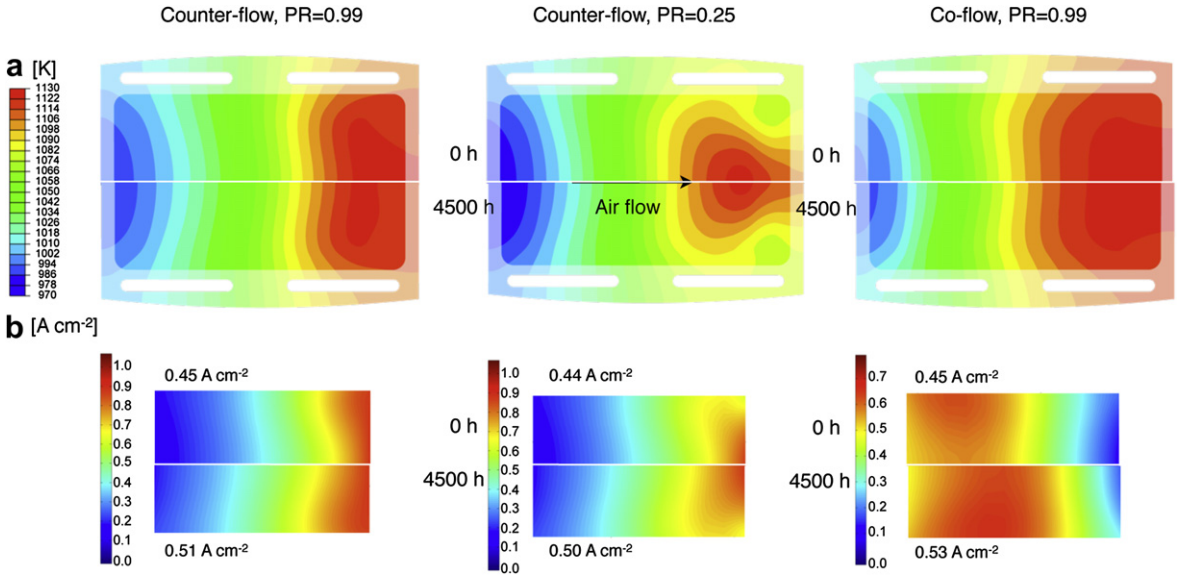

Fig. 3 – (a) Temperature profile and (b) current density at start (above symmetry lines) and after 4500 h of operation (below symmetry line) at a system specific power of 0.29 W cm^{-2} and maximum solid temperature of 1125 K in a SRU with C1 cell.

4. Results and discussion

4.1. Cell failures

Results from Case 1 and Case 2 (see Section 3) show the separate effects on the cell probability of failure of (i) the modification of the temperature profile due to electrochemical degradation and (ii) creep deformation of the SRU components, except the MEA.

4.1.1. Effect of the modification of the temperature profile because of electrochemical degradation (Case 1)

During operation at constant system specific power, fuel utilisation, air inlet temperature and maximum SRU temperature, the current density and air ratio must be ever increased to compensate the electrochemical degradation (see Fig. 2 and [43,44] for a dedicated analysis). This results in minor modifications of the temperature profile. The SRU solid temperature at the air inlet zone tends towards the fixed air inlet temperature as the air ratio is increased. In the conditions treated here, the degradation of the cathode due to chromium contamination dominates in the long term. The cathode local overpotential mainly governs the rate of deposition of Cr_2O_3 at the TPB from $CrO_2(OH)_{2(g)}$ released by the MIC. Its distribution differs in co- or counter-flow configuration. Fig. 3 shows that in co-flow, the location of highest current density follows a trade-off between high temperature and hydrogen-rich anode gas, available air outlet and air inlet sides, respectively, of the active area. Contamination preferentially affects the fuel inlet of the active area because the cathode local overpotential is the highest at this location. It progressively shifts the maximum current density towards the fuel outlet side of the cell. In counter-flow, high temperature and hydrogen-rich anode gas are available at the fuel inlet zone of the active area. The cathode local overpotential is the highest at this location but its distribution is more even and its maximum lower than in the co-flow case, which alleviates degradation. The current density profile flattens as chromium contamination proceeds, which results in a less pronounced peak of temperature at the air outlet side of the GDL, along the symmetry line, that is most evident for low methane conversion fractions in the reformer.

Fig. 4a shows the evolution of the probability of failure of the anode due to the modification of the temperature profiles induced by electrochemical degradation, for the co- and counter-flow configurations (Case 1). The predicted probabilities of failure are low in general. The set of Weibull parameters for the strength of the anode that is the closest to the case treated in the electrochemical degradation simulations was selected for this study. The analysis performed in Ref. [42] has shown that achievable material improvements, such as a Weibull modulus exceeding 10 combined with a characteristic strength of 90 MPa in similar strength test conditions, provide a sufficient reliability for a prototype. State-of-the-art anodes may have already reached this target, which lies within the 95% confidence interval of the anode data used here.

Table 3 lists the ratio between the computed probabilities of failures at start and after 4500 h of operation at a system

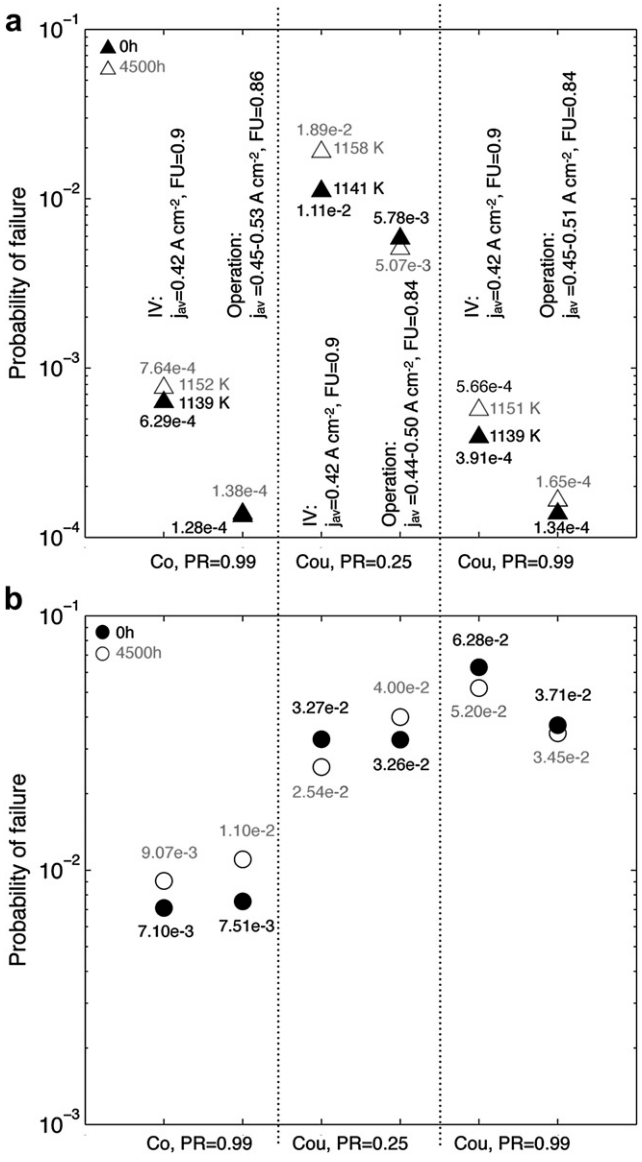

Fig. 4 – (a) Anode and (b) cathode probability of failure during IV characterisation and nominal operation (Case 1, GSK and C1 cell), at the initial time and after 4500 h of operation at constant system specific power of 0.29 W cm^{-2}, for the co-flow (PR = 0.99) and counter-flow configuration (PR = 0.25 or PR = 0.99).

specific power of 0.29 W cm^{-2}. These computed factors are provided to facilitate the comparison between the different simulated cases only. Their applicability to any situation is prevented among others by the current limited knowledge of the mechanical properties of SOFC stack materials, by the incomplete understanding of the degradation processes and by the variety of stack designs and possible SOFC system operation modes.

Long-term operation causes an increase of the cell layer probability of failure at the end of the IV characterisation (FU = 0.9) for all cases (see Fig. 4a), because for fixed gas inlet conditions, electrochemical degradation amplifies the

Table 3 – Computed factors on the anode and cathode probability of failure in operation at constant system specific power, due to electrochemical degradation (Case 1, 4500 h) and creep in the components, except the cell layers (Case 2, GSK and GLS, 5500 h). Inside parentheses are the values during IV characterisation.

		Co, PR = 0.99	Cou, PR = 0.25	Cou, PR = 0.99
Electrochem. degr. (Case 1, GSK)	Anode	1.08 (1.21)	0.88 (1.70)	1.23 (1.45)
	Cathode	1.46 (1.28)	1.23 (0.78)	0.93 (0.83)
Creep (GSK, Case 2)	Anode	1.09 (1.11)	1.04 (1.05)	1.28 (0.99)
	Cathode	1.02 (1.03)	1.02 (1.04)	1.02 (1.02)
Creep (GLS, Case 2)	Anode	0.02	1.25	0.05
	Cathode	4.13	5.25	136

maximum and pattern specificities of the SRU temperature profile. In the conditions considered here, electrochemical degradation affects the computed anode probability of failure by a factor up to 1.7 (see Table 3), whereas the choice of operating conditions induces variations exceeding one order of magnitude. Cell failure can, however, arise from load following or characterisation procedures that neglect degradation. Spatial temperature control is relevant to mitigate such harmful situations [64]. During operation at constant system specific power, the computed probability of failure of the anode increases for completely pre-reformed anode gas, by up to approximately 20%. In counter-flow combined with a methane conversion fraction of 0.25, the increase of the air/fuel ratio needed to keep the maximum SRU temperature constant as electrochemical degradation proceeds is beneficial for the cell mechanical reliability, since it limits the extent of the zone of higher temperature that develops at the air outlet of the active area (see Fig. 3).

The temperature dependence of the CTE mismatch between the cathode and the anode governs the evolution of the probability of failure of the cathode. It causes a change in stress from tensile to compressive in the cathode, depending upon the temperature, the most critical range being around 973 K and the threshold temperature being around 1073 K in the case treated here [23,46]. The detrimental effect of electrochemical degradation is comparable in magnitude for the anode and the cathode (Fig. 4b and Table 3). During operation in co-flow configuration, the displacement of the maximum current density towards the fuel outlet direction, as chromium contamination preferentially affects the cathode active area towards the fuel inlet, combined with the increase of the air ratio, increase the risks of cathode failure, since a larger volume of cathode material is exposed to temperatures below the threshold temperature (approx. 1073 K). In counter-flow, chromium that deposits preferentially at the fuel inlet side in the cathode and the increase of the air ratio have an opposite effect on the evolution of the temperature profile. For a methane conversion fraction of 0.25, the increase of the air ratio to maintain a maximum solid temperature of 1125 K, rather than the redistribution of the current density because of the cathode degradation, governs the evolution of the temperature profile (see Fig. 3). The volume of cathode subjected to temperatures below the threshold temperature therefore increases and so does the cathode probability of failure. In contrast, for a methane conversion fraction of 0.99, the redistribution of the current density causes a slight increase of the average temperature in the cathode, the

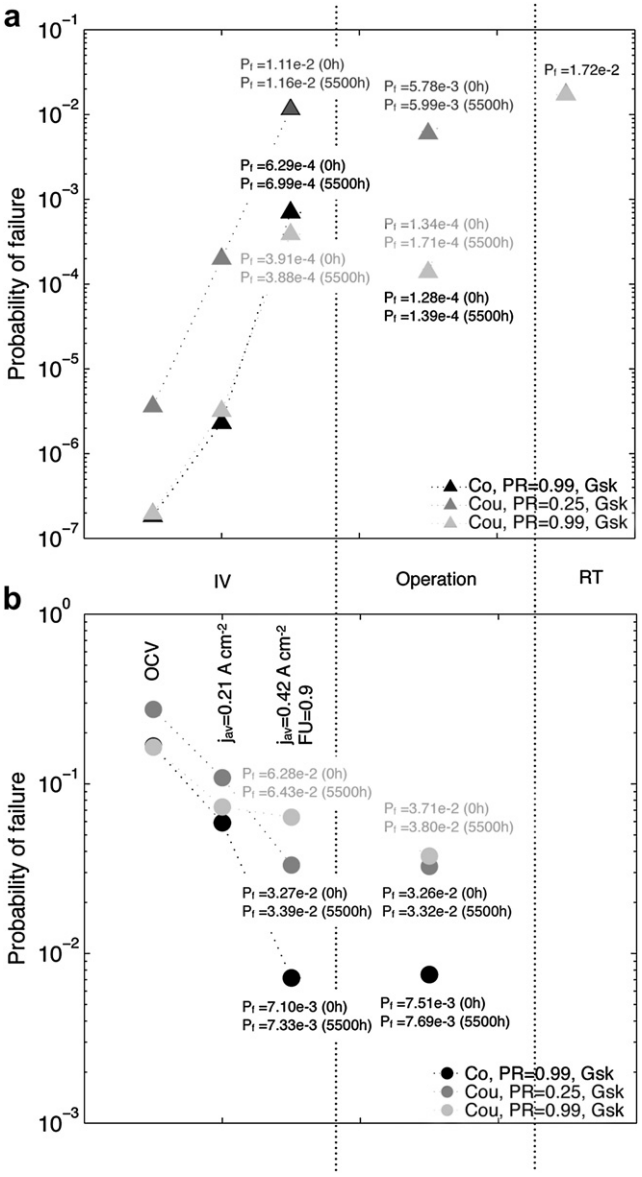

Fig. 5 – Evolution of (a) the anode and (b) cathode probability of failure during IV characterisation, operation at constant system power of 0.29 W cm^{-2} with creep of the GDL and MIC and thermal cycle to room temperature (Case 2, GSK, C1), for the co-flow (PR = 0.99) and counter-flow (PR = 0.25 and 0.99) configurations.

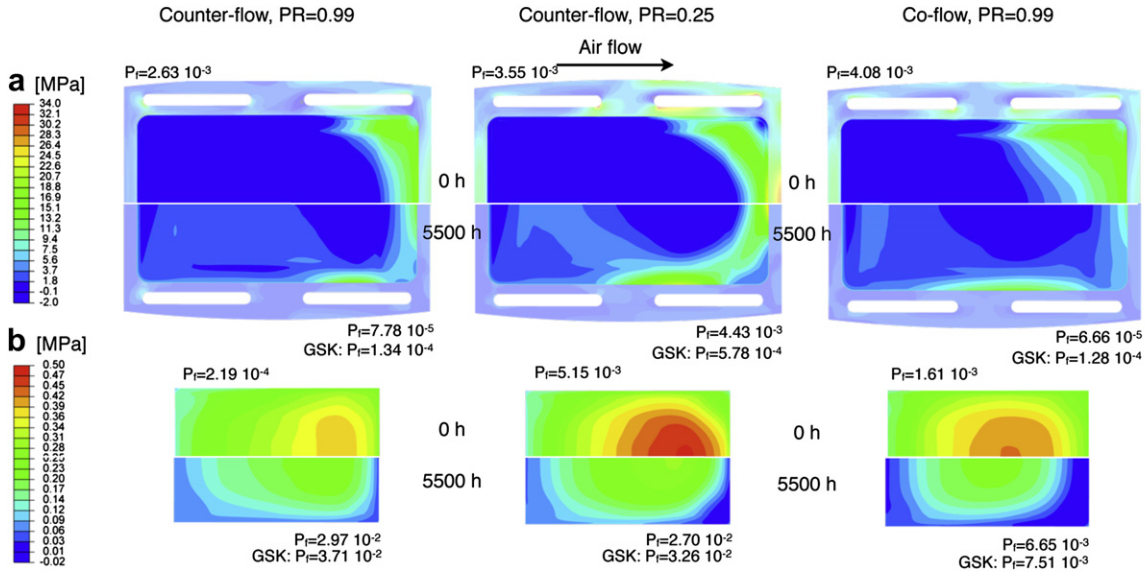

Fig. 6 – (a) First principal stress in the anode and (b) contact pressure on the cathode GDL. The profile above the symmetry line refers to t = 0 h, that below the symmetry line to 5500 h of operation at constant system power of 0.29 W cm^{-2} (Case 2, GLS). The temperature profiles in operation are those in Fig. 3.

probability of failure of which consequently decreases. The volume of cathode material subjected to temperatures lower than the threshold temperature at a fuel utilisation of 0.9 increases (decreases) in co-flow (counter-flow). The cathode probability of failure varies accordingly.

4.1.2. *Effect of creep deformation in components other than the cell (Case 2)*

Simulations performed in Case 2 show that creep deformation of the MIC and GDLs, in the case of compressive gaskets (GSK), has a smaller influence than electrochemical degradation on cell mechanical failure. The computed probabilities of failure are affected by factors between slightly less than 1 and 1.3 (Table 3).

Fig. 5 depicts the evolution of the anode probability of failure during (i) the IV characterisation, (ii) operation and (iii) thermal cycle to room temperature. Values are indicated, because the difference amongst the results for the sequences performed at different times is hardly visible. Stress develops in the anode during the IV characterisation as current is drawn from the stack. Thermal cycling to RT generates the most detrimental conditions for the structural integrity of the anode and is barely affected by electrochemical degradation (not depicted) and creep in the SRU components other than the cell. The Weibull parameters for the strength of the anode support at high temperature and reduced state could not be found for a given material [25]. Identical values have been consequently used at high and room temperature, which may imperfectly reflect the reality and prevents a direct comparison.

In the conditions of Case 2 with compressive gaskets (GSK), creep deformation of the MIC and GDLs induces very subtle changes in the stress distribution in the cell, which does not allow unambiguous identification of the reasons for the slight modifications in cell probability of failure. It may however indirectly cause cell failure, since it provokes a detrimental loss of contact pressure at specific locations on the GDLs and SRU deformation, which is the subject of Section 4.2.

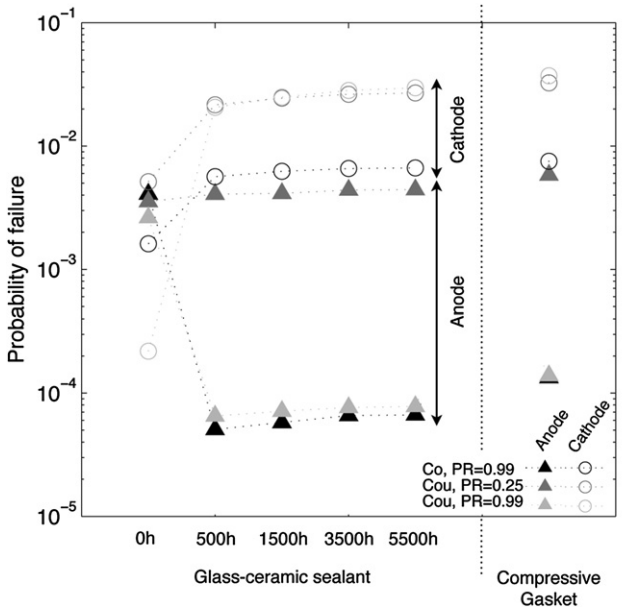

Fig. 7 – Evolution of the anode (filled triangles) and cathode (empty circles) probabilities of failure during operation at the nominal point with creep of the GDLs, MICs and glass-ceramic sealants (Case 2, GLS, C1 cell), for the co-flow (PR = 0.99) and counter-flow configurations (PR = 0.25, PR = 0.99). The starting point is after the initial annealing time of 10 h. The probability of failure for the case of compressive gaskets is provided for comparison.

The evolution of the probability of failure of the cathode during the sequence simulated here is opposite to that of the anode, because of the predominant influence of the temperature dependence of the CTE mismatch between the cathode and the anode. The risk of failure is the highest at OCV conditions since the whole cathode withstands tensile stress. It then decreases as the temperature increases and passes the threshold temperature during IV characterisation and operation. It vanishes at room temperature, because the cathode withstands compressive stress, from approximately 573 K, in the range of 10 MPa at RT, which cannot alone induce buckling-driven delamination [23].

In Case 2, the glass-ceramic sealant (GLS) amplifies the mechanical interactions between the SRU components. Fig. 6 shows the evolution of the first principal stress in the anode as creep proceeds in the MIC, GDLs and glass-ceramic sealant. Fig. 7 depicts the corresponding probabilities of failure. The CTE mismatch between the anode and the MICs is more pronounced in the temperature range from 973 to 1073 K (Crofer22APU: 11.6 $\times$ 10^{-6} K^{-1}, Ni-YSZ: 12.4 $\times$ 10^{-6} K^{-1} on average) than at higher temperature (Crofer22APU: 12.0 $\times$ 10^{-6} K^{-1} at 1123 K). In all cases, the CTE mismatch initially protects the anode in the lower temperature region, until the first half of the SRU from the air inlet side, whereas tensile stresses develop in the zones of higher temperature.

In the long-term, the stress distribution becomes similar to that observed with compressive gaskets (compare Fig. 6 with Fig. 12 later) and so do the anode probabilities of failure. The decay observed mostly during the first 500 h of operation, with completely pre-reformed fuel exceeds one order of magnitude and passes through a minimum. In counter-flow with internal reforming the computed anode probability of failure slightly increases, by a factor of 1.25 (Table 3). In contrast, the stress in the cathode is compressive in the high temperature zone, because of the predominant effect of the CTE mismatch with the anode. The compressive constraint on the cell induced by the previously mentioned CTE mismatch between the anode and MIC materials is beneficial for the cathode as well. The cathode probability of failure therefore increases as creep in the metallic and glass-ceramic components proceeds.

Fig. 8 depicts the evolution of the maximum first principal stress in the glass-ceramic sealant, and von Mises stress in the MIC, during operation, interrupted with thermal cycles. The maximum stresses decrease at high temperature but increase at room temperature and OCV because of the irreversible deformation. The glass-ceramic seal likely fails at RT and OCV, because the stress around 70 MPa and 16 MPa, respectively, are close to or exceed the strength of the material (see Table 1). Similarily, the Weibull analysis indicates the failure of the anode during thermal cycling to RT for the GLS case (not depicted). In reality, stress relaxation during the cooldown, which is not included in the analysis, may alleviate the risks of cell failure. This underscores the need for investigations on the impact of the cooling/heating ramps, including the evolving temperature profile during electrical load shut-down and cooldown to room temperature.

Fig. 8 shows that the stress in the MIC during the initial thermal cycle is significantly lower with compressive gaskets than glass-ceramic sealant, since in the former case, only friction prevents the complete accommodation of the CTE

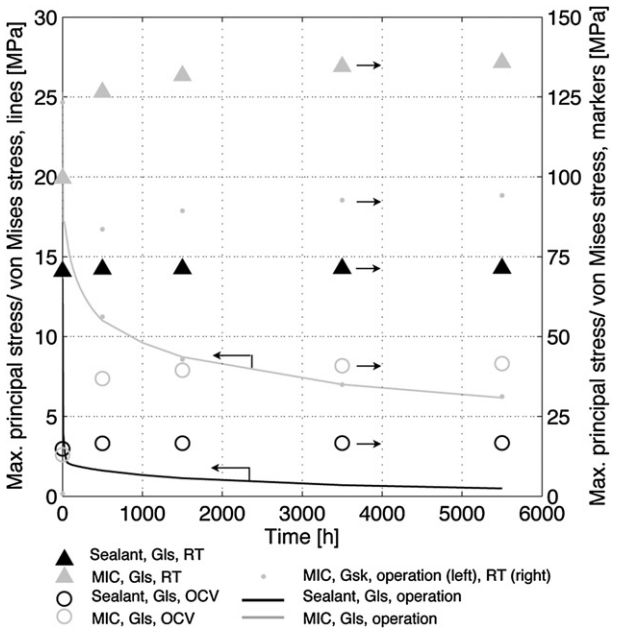

Fig. 8 – Evolution of the maximum first principal stress in the glass-ceramic sealant and maximum von Mises stress in the MIC, at high temperature with a fixed temperature profile (lines), during thermal cycling to room temperature (filled triangles) and IV characterisation (OCV, empty circles) with a C1 cell. The maximum von Mises stress in the MIC, for the GSK case, is provided for comparison (dots).

mismatches. Irreversible deformation is generated at high temperature in operation, which induces additional stress at other conditions, such as OCV or RT. However, the high values (100–135 MPa at RT, 42 MPa at OCV) do not exceed the elastic limit of the material of 268 MPa at RT, around 90 MPa at OCV.

Lowering the system specific power increases the lifetime and consequently the time scale for the effects of the electrochemical degradation on mechanical reliability. It would only marginally modify the trends induced by creep of the SRU components, since in this case, the reliability of the predicted time scales depends on the accuracy of the material mechanical properties implemented in the model. More SRUs must be stacked to achieve a specified system power, which, from the prospect of mechanical reliability, increases the volume of brittle ceramic material and issues arising from the difficulty of ensuring the reproducibility of components mechanical properties.

4.2. *Evolution of the contact pressure on the gas diffusion layer (Case 2)*

The Weibull analysis in Section 4.1 highlights the limited effect of the evolution of the temperature profile due to electrochemical degradation and of creep of the metallic parts on the probability of failure of the cell, in the case of compressive gaskets.

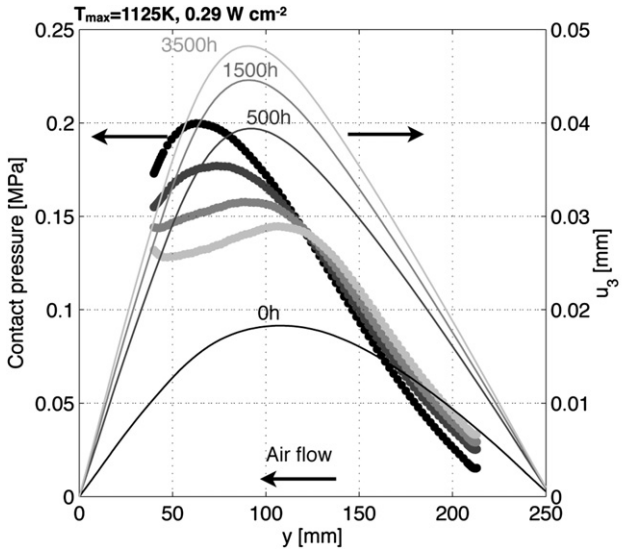

Fig. 9 – Evolution of MIC deflection and contact pressure on the cathode GDL, for the counter-flow configuration (PR = 0.25), with C1 cell and GSK sealants.

A severe loss of electrical contact at a single interface can provoke the end of life of a SOFC stack, because of the in-series electrical assembly of the SRUs. Local high electrical contact resistances can indirectly promote cell cracking, through modifications of the temperature profile or activation of the regime of accelerated degradation of the performance of a SOFC stack implemented in a system, as shown e.g., in Refs [43,44,65]. At present, the lack of knowledge on the mechanical properties of the GDL materials and contacting pastes, and the exact nature of the mechanical interactions at the interfaces [66,67] prevents comprehensive structural analyses. The approach pursued here is to identify the conditions that cause the local loss of the desirable and properly controlled compressive contact stress at the GDL interfaces. The case of the cathode GDL is displayed, because in anode-supported cells contacting issues are typically more critical on the cathode side, because of the lower electrical conductivity of the materials and lower electrode thickness, which amplifies current constriction issues.

Fig. 9 illustrates the evolution of the MIC deflection and contact pressure on the cathode GDL, due to creep in the MIC and GDLs (Case 2) along the symmetry line, for the counter-flow configuration. The profile follows that of the temperature profile (see Fig. 3a). The increase in deflection slows as

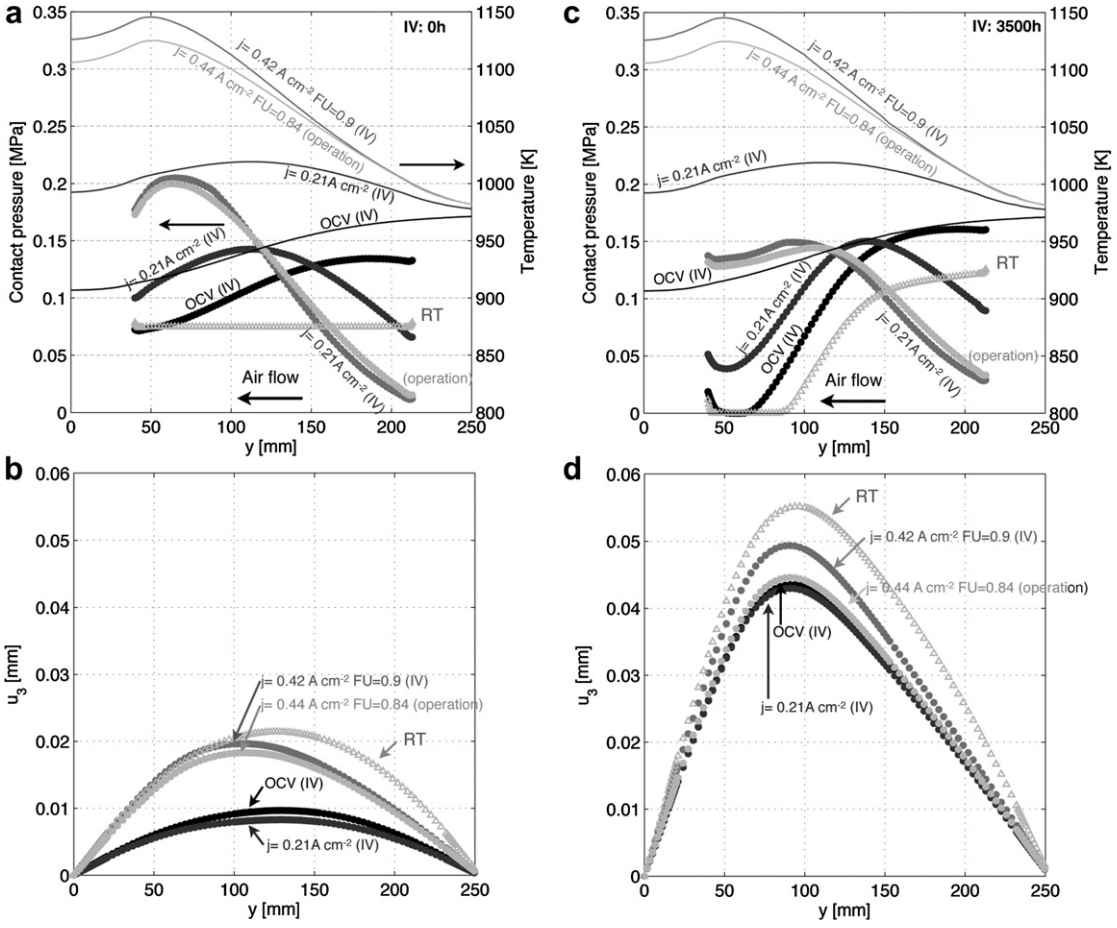

Fig. 10 – Evolution of (a,c) the contact pressure on the cathode GDL and temperature profile and (b,d) lower MIC deflection along the symmetry axis, during an IV characterisation and thermal cycle to RT. (a,b) refer to the initial time and (c,d) after 3500 h of operation (COU, PR = 0.25, C1 cell, GSK sealants).

operating time increases. It doubles during the first 500 h. The driving force is the residual stress in the cell, which preferentially acts at the locations where the creep strain rate in the other components is the highest. Therefore, the position of maximum displacement along the z-axis moves towards the air outlet, where the temperature and compressive stress are higher. Creep deformation in the anode GDL flattens the distribution of the contact pressure. The trends are similar for the other flow configuration and methane conversion fraction in the reformer (not depicted).

The non-uniform irreversible strains generated in the metallic components in operation induce a history-dependent behaviour. Fig. 10 compares the evolution of the MIC deflection and contact pressure on the cathode GDL during IV characterisation and thermal cycling to RT performed at the initial time and after 3500 h of operation (Case 2). The drastic modifications of the predicted contact pressure distribution are in line with the difficulty of recovering the electrical contact in a damaged SOFC stack that have been observed at LENI-EPFL by increasing, for instance, the furnace temperature and assembly load. The contact pressure is initially compressive over the whole GDL. The irreversible deformation generated in the anode GDL in the zone of highest temperature and compressive stress during operation induces after 3500 h a loss of contact pressure at OCV, and RT, which may alter the electrical contact. The loss of contact pressure at OCV suggests that following of the electrical load demand or setting at idling conditions during prolonged periods can shorten the operating lifetime of a SOFC stack. Operation in co-flow with pre-reformed feed anode gas produces similar

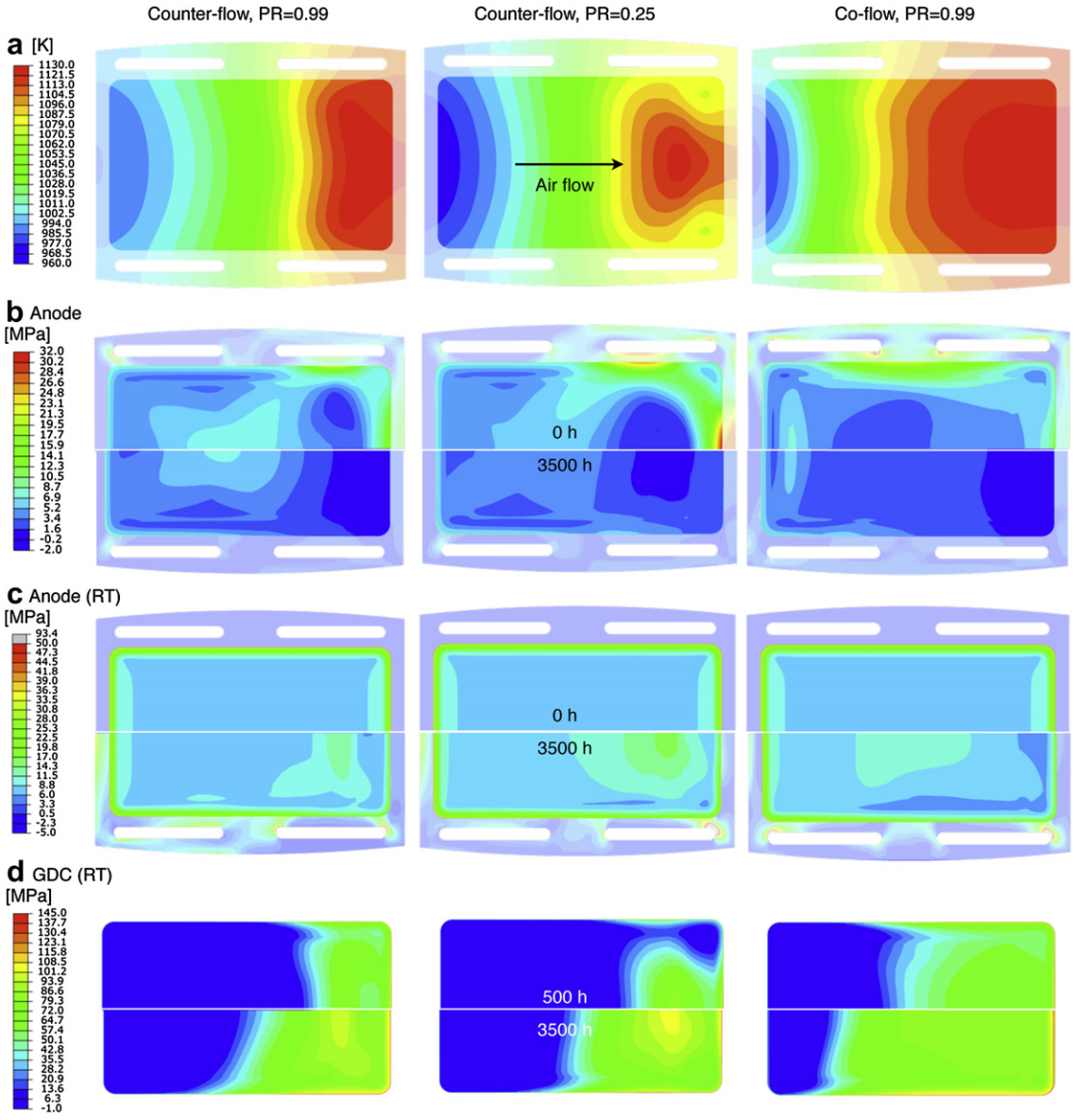

Fig. 11 – Effect of creep in the C2 cell and (a) temperature distribution, on (b) the evolution of the first principal stress in the anode support in operation and (c) during thermal cycling to RT and (d) evolution of the first principal stress in the GDC compatibility layer at room temperature. The profiles above and below the symmetry axis refer to different operation time (Case 3, GSK sealants).

trends, even though the size of the zone where the contact pressure is lost is smaller.

The deflection of the SRU is irreversibly modified. The variation between the investigated conditions, i.e., operation, IV characterisation and RT decreases with operating time, since the distribution of the creep deformation is generated for the temperature profile in operation. The Young's modulus of the MIC material (see Table 1) and the residual stress in the cell have opposite temperature dependences. The results suggest that both effects compensate each other, since the deflection does not drastically differ at operating and room temperature.

4.3. *Creep of the cell layers and shrinkage of the anode during thermal cycling (Case 3 and Case 4)*

Creep in the MEA layers lowers the magnitude of the stresses, and consequently the probability of failure of the cell at operating temperature, if the strength of the layers stays constant. Case 3 and Case 4 are used for the analysis in this section. Shielding compressive residual stresses in the electrolyte and compatibility layer, in the case of LSCF cathode, that are beneficial for redox tolerance, among other reasons, are relieved as well. Changes in stress state in some layers can consequently arise from the temperature dependence of the CTEs combined with creep deformation, if a drastic variation in operating conditions is applied to the SOFC stack.

Fig. 11 depicts the evolution of the stress in the anode support and GDC compatibility layer of a C2 cell (LSCF cathode) subjected to combined operation (Case 3) and thermal cycling. The stress in the anode support decreases during operation (see Fig. 11b). During thermal cycling, the magnitude of the tensile stress in the zones subjected to compressive stress during operation increases (see Fig. 11c). The GDC compatibility layer initially withstands compressive stress, that is relieved during operation. Fig. 11d shows how the stress state turns from compressive to tensile at room temperature, after prolonged operation, because of the difference in CTEs amongst the cell layers. Due to the temperature dependence of the creep strain rate, the zone of tensile stress progressively spreads. The highest value develops in the counter-flow configuration, because the zone of localised higher temperature is more pronounced. There, the stress in the GDC compatibility layer of approximately 100 MPa exceeds the value of 58 MPa that is computed with a model based on the Euler-Bernoulli theory [23]. The characteristic strength of GDC at room temperature, in the range of 134–143 MPa [68] will lead to a high probability of failure of this layer. The time to change the stress state depends upon the mechanical properties of all layers. The prediction here of

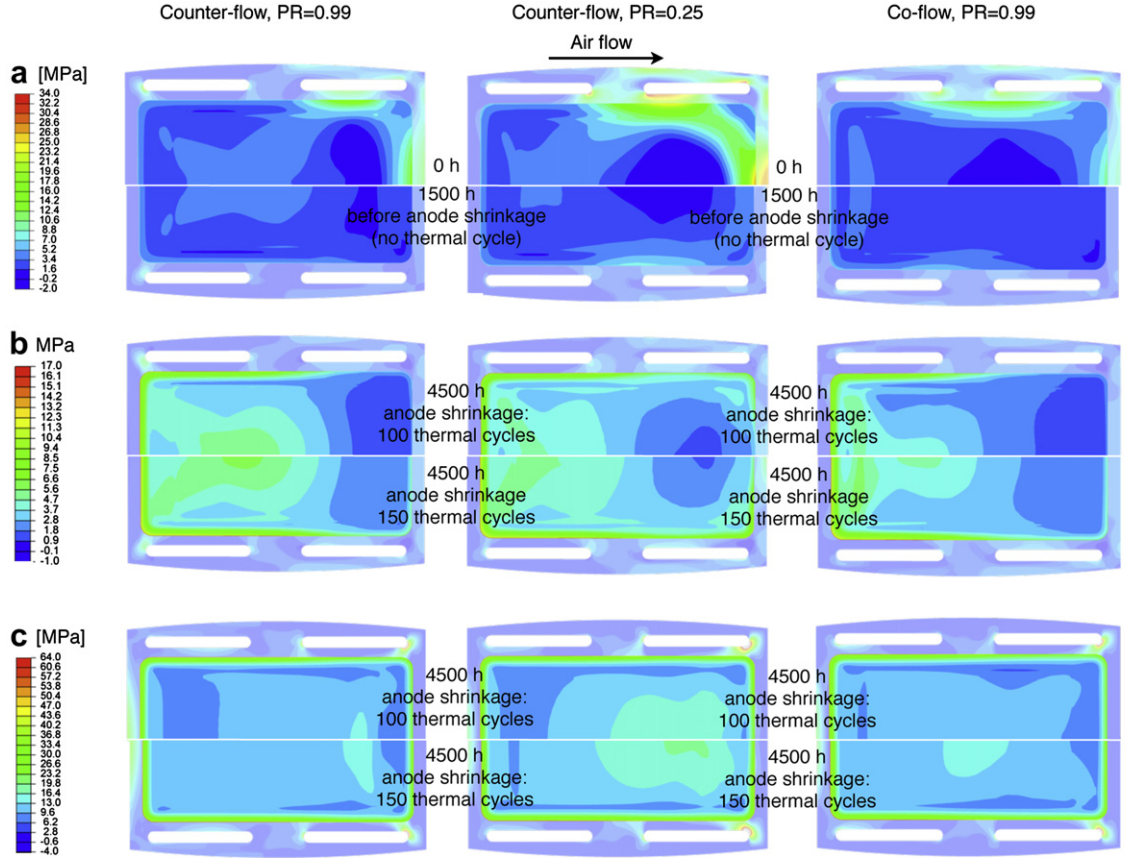

Fig. 12 – Effect of creep and anode shrinkage in the C1 cell (Case 4) on (a) the evolution of the first principal stress in the anode support in operation before anode shrinkage, (b) after anode shrinkage, corresponding to 100 and 150 thermal cycles and (c) at room temperature before and after 100 and 50 cycles. The profiles above and below the symmetry axis refer to different operation time. Co- or counter-flow configuration (PR = 0.99) with GSK sealants. The temperature profiles in operation are those in Fig. 3.

less than 500 h is qualitative and limited above all by the limited data on the creep behaviour of the MEA materials.

The data on the long-term and high temperature behaviour of the Ni-YSZ anode support [15,18–20,69] remains sparse and, most of the time, not extensive enough for modelling studies. The underlying mechanisms that lead to its shrinkage during thermal cycling are not completely understood [19,20]. The variety of conditions in a stack in operation and progressive coarsening of the nickel particles may modify locally the mechanical properties of the anode.

Case 4 allows the investigation of the combined effect of anode shrinkage and creep in the MEA layers. Fig. 12a shows the relief of stress in the anode of a C1 cell during operation. After combined prolonged operation and thermal cycling (4500 h and 100 cycles in Fig. 12b), the tensile stress on the lateral and air outlet sides of the anode, due to the zone of higher temperature significantly decreases, whereas the stress in the zone of lower temperature increases.

Under the present model assumptions, the magnitude of the stress depends upon the ratio between thermal cycles, i.e., equivalently anode shrinkage, and high temperature operation time to relieve the stress. The resistance of an anode towards thermal cycling is likely strongly dependent on the microstructure and partial thermal cycling may also induce shrinkage. Therefore, extreme conditions have been simulated here (292 cycles per year of high temperature operation). The need to specifically mitigate such a phenomenon therefore depends upon the foreseen application of the stack. Fig. 12c shows that the stress distribution at room temperature remains qualitatively unaltered, because of the uniform shrinkage. The non-uniformity arises from the creep deformation generated in operation, as discussed previously for the C2 cell.

Fig. 13 shows the effect of anode shrinkage on the SRU deflection. At each thermal cycle, the implementation of the anode shrinkage induces an increase of the deflection, which is comparable each time. The contact pressure at room temperature is subjected to the issues discussed in Section 4.2 but is not significantly affected by the shrinkage of the anode.

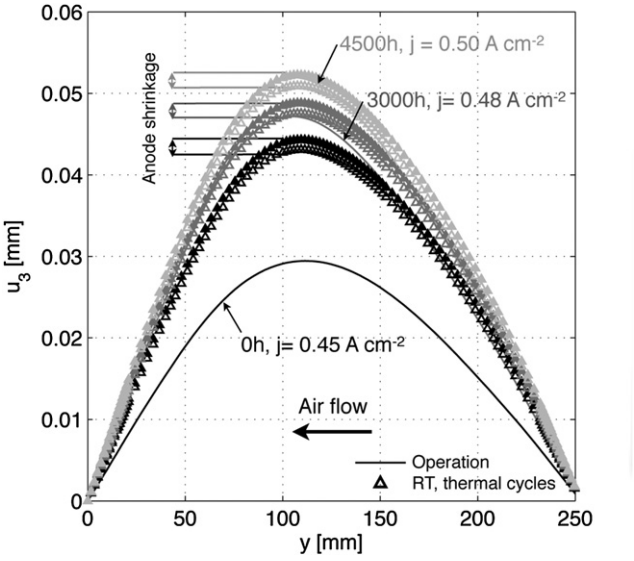

Fig. 13 – Evolution of the deflection of the lower MIC during operation (lines, Case 4) and thermal cycling, before (empty markers) and after (filled markers) the shrinkage of the anode support. C1 cell, GSK sealants.

The experimentally measured shrinkage of the anode support [19] can significantly affect the distribution of stress in the anode support. To circumvent its effect, dedicated experiments are needed to first understand, and then model the underlying mechanisms, including the ascertained dependence on heating and cooling, and probable dependence on temperature and anode gas composition. The foreseen application of the stack determines the ratio between number of thermal cycles and operating time at high temperature. This information is however not sufficient to propose reliable mitigation approaches. Indeed, even though a Weibull analysis with existing data can be easily performed on the simulation results presented in this section, its validity would be questionable. The apparent strength of a composite that exhibits non-negligible irreversible deformation probably differs from that of the nascent one.

5. Conclusion

This study has investigated how electrochemical degradation and creep of the SRU components and shrinkage of the anode support affect the mechanical reliability of SOFC stacks under practical system operating conditions. This study enlarged with structural analysis our previous studies on the effects of the operating conditions on the degradation of a SOFC stack [43,44].

The current (i) knowledge on the mechanical stability of SOFC stack materials, (ii) knowledge on the processes that cause electrochemical degradation and (iii) difficulty to find experimental data from SOFC stack tests under appropriate conditions for model calibration prevents providing fully reliable guidance. The quantitative information generated in the present study, such as the factors on the probability of failure, is for comparison purpose. The direct use for other designs of the geometrical and material options and operating conditions highlighted in the present study also requires care. Subtle changes in the mechanical properties of the materials and interactions between the components govern the failure modes. Furthermore, the system layout influences the optimal SOFC stack operating conditions, therefore the processes predominantly affecting electrochemical degradation.

In the conditions treated here, both anode and LSM-YSZ cathode contribute to the cell probability of failure, provided by Weibull analysis. The determination of the most critical layer can be calculated, but practically suffers from the large confidence intervals for the Weibull parameters, that cause scatter in the range of one to several orders of magnitude. The modification of the temperature profile caused by electrochemical degradation during operation at constant system power modifies the probability of failure of the cell depending upon the operating conditions. The computed factors range from 0.9 up to 1.7 for the anode and from 0.8 up to 1.5 for the cathode after 4500 h at a constant system specific power of 0.29 W cm^{-2}. The effect is smaller than the choice of operating conditions, which can exceed one order of magnitude, and negligible on the probability of failure during thermal cycling

to room temperature. The highest increases occur during IV characterisation procedures. This suggests that detrimental evolution of the temperature profile can induce unexpected failure if the control strategy during following of the electrical load demand is not adapted in the long-term for degradation.

Because of different levels of mechanical interaction between the components, the direct influence of creep deformation on the integrity of the cell is significant with glass-ceramic sealants (computed factors of 0.02 up to 1.3 for the anode probability of failure, and 4 to 136 for that of the cathode), and limited with compressive sealing gaskets (computed factor of slightly less than 1 up to 1.3). In the former case and for completely pre-reformed fuel, the anode probability of failure passes through a minimum around 500 h and tends towards that predicted for compressive sealing gaskets. Failure of the sealant is likely during thermal cycling and may be triggered by a rapid change from operation to OCV conditions.

The residual stress in the cell and creep relaxation in the MIC, increases in the long-term the deflection of a SRU in a stack. Therefore the initial maximum value in the range of 20–30 μm approximately for compressive gaskets almost doubles after 500 h at operating temperature. The evolution is afterwards less pronounced over time in operation. The SRU deflection does not drastically affect the cell probability of failure, but contributes, together with the uneven irreversible deformation generated in the GDLs, to exacerbate the history-dependence of the contact pressure on the cathode GDL. The latter flattens during operation at constant system specific power. Significant modifications of the conditions, such as those encountered during thermal cycling or setting at OCV, yield complete relief of the contact pressure in the zone near the air outlet side, where the creep strain rate is the highest in operation. Definitive damage may be generated, but the current knowledge of the bulk and interfacial mechanical properties of the GDL cannot support a completely reliable analysis.

The GDC compatibility layer in a cell based on a LSCF cathode is potentially very vulnerable to thermal cycling. Critical tensile stress progressively develops in this layer at room temperature, after operation, because of the relief of the shielding compressive stress by creep during operation. The shape of the temperature profile in operation results in an increase of the stress in the GDC layer at room temperature of more than 50 MPa, compared with the case of uniform temperature. The zones of highest tensile stress in the anode at room temperature are those subjected to compressive stress in operation, because of creep deformation.

The shrinkage of the anode support material during thermal cycling may exceed the relief of the stress in the anode by creep during operation, depending upon the thermal cycling frequency a SOFC stack must incur. The tensile stress in the high temperature zones is relieved, whereas that in the cold ones increases.

The model predicts the detrimental impact of electrochemical degradation, variations of the operating conditions and thermal cycling on the risks of failure, that overall progressively increase during prolonged use. This capability warrants further investigations to quantitatively predict the detrimental effects and the risks associated to thermal cycling and complex operation modes such as load following. Besides the need for experimental data on the mechanical properties of the materials under appropriate conditions and experimental data from SOFC stack tests for model calibration, improvements of the modelling framework are needed for such tasks. The submodelling procedure must be modified to cope with creep in the MEA layers. The level of coupling between thermo-electrochemical and mechanical aspects, currently restricted to discrete importing of the temperature profile, must be increased to address the complexity of this real situation.

Acknowledgements

This work was funded by the Swiss SOFC Consortium, co-financed by the Swiss Federal Office of Energy (SFOE) and Swisselectric Research, contract number 152210, and the FP6 FLAMESOFC European project, contract number CE-Flame SOFC-019875. The authors would like to thank Dr. Cugnoni (LMAF-EPFL) for all his useful advices. Prof. T. Kawada (Tohoku University) is kindly acknowledged for careful reading of the manuscript. gPROMS, a modelling tool from Process System Enterprise (PSE) and ABAQUS from Simulia have been used under academic licensing. Computations have been performed on the Pleiades2 cluster located at EPFL.

REFERENCES

[1] Kuebler J, Vogt UF, Haberstock D, Sfeir J, Mai A, Hocker T, et al. Simulation and validation of thermo-mechanical stresses in planar SOFCs. Fuel Cells 2010;10(6):1066–73.
[2] Wuillemin Z, Autissier N, Nakajo A, Luong MT, Van herle J, Favrat D. Modeling and study of the influence of sealing on a solid oxide fuel cell. Journal of Fuel Cell Science and Technology 2008;5(1):011016–9.
[3] Diethelm S, Van herle J, Wuillemin Z, Nakajo A, Autissier N, Molinelli M. Impact of materials and design on solid oxide fuel cell stack operation. Journal of Fuel Cell Science and Technology 2008;5(3):1–6. 031003.
[4] Malzbender J, Steinbrech R, Singheiser L. A review of advanced techniques for characterising SOFC behaviour. Fuel Cells 2009;9(6):785–93.
[5] Hagen A, Hendriksen PV, Frandsen HL, Thydén K, Barfod R. Durability study of SOFCs under cycling current load conditions. Fuel Cells 2009;9(6):814–22.
[6] Dikwal C, Bujalski W, Kendall K. The effect of temperature gradients on thermal cycling and isothermal ageing of micro-tubular solid oxide fuel cells. Journal of Power Sources 2009; 193(1):241–8.
[7] Liu Y, Hagen A, Barfod R, Chen M, Wang H, Poulsen F, et al. Microstructural studies on degradation of interface between LSM-YSZ cathode and YSZ electrolyte in SOFCs. Solid State Ionics 2009;180(23–25):1298–304.
[8] Hagen A, Liu YL, Barfod R, Hendriksen PV. Assessment of the cathode contribution to the degradation of anode-supported solid oxide fuel cells. Journal of the Electrochemical Society 2008;155(10):B1047–52.
[9] Simwonis D, Tietz F, Stöver D. Nickel coarsening in annealed Ni/8YSZ anode substrates for solid oxide fuel cells. Solid State Ionics 2000;132(3–4):241–51.
[10] Tanasini P, Cannarozzo M, Costamagna P, Faes A, Van herle J, Hessler-Wyser A, et al. Experimental and theoretical

investigation of degradation mechanisms by particle coarsening in SOFC electrodes. Fuel Cells 2009;9(5):740–52.
[11] Faes A, Hessler-Wyser A, Presvytes D, Vayenas C, Van herle J. Nickel-Zirconia anode degradation and triple phase boundary quantification from microstructural analysis. Fuel Cells 2009;9(6):841–51.
[12] Holzer L, Iwanschitz B, Hocker T, Münch B, Prestat M, Wiedenmann D, et al. Microstructure degradation of cermet anodes for solid oxide fuel cells: quantification of nickel grain growth in dry and in humid atmospheres. Journal of Power Sources 2011;196(3):1279–94.
[13] Holzer L, Münch B, Iwanschitz B, Cantoni M, Hocker T, Graule T. Quantitative relationships between composition, particle size, triple phase boundary length and surface area in nickel-cermet anodes for solid oxide fuel cells. Journal of Power Sources 2011;196(17):7076–89.
[14] Menzler NH, de Haart LG, Sebold D. Characterization of cathode chromium Incorporation during mid-term stack operation under various operational conditions. ECS Transactions 2007;7(1):245–54.
[15] Lara-Curzio E, Radovic M, Trejo M, Cofer C, Watkins T, More K. Effect of thermal cycling and thermal aging on the mechanical properties of, and residual stresses in, Ni-YSZ/YSZ bi-layers. Advances in Solid Oxide Fuel Cells II 2007; 27(4):383–91.
[16] Kuebler J, Primas R, Gut B. Mechanical strength of thermally aged and cycled thin zirconia sheets. Adv Sci Technol 3 B; 1994.
[17] Faes A, Nakajo A, Hessler-Wyser A, Dubois D, Brisse A, Modena S, et al. Redox study of anode-supported solid oxide fuel cell. Journal of Power Sources 2009;193(1):55–64.
[18] Pihlatie M, Frandsen H, Kaiser A, Mogensen M. Continuum mechanics simulations of NiO/Ni-YSZ composites during reduction and re-oxidation. Journal of Power Sources 2010; 195(9):2677–90.
[19] Mori M, Yamamoto T, Itoh H, Inaba H, Tagawa H. Thermal expansion of nickel-zirconia anodes in solid oxide fuel cells during fabrication and operation. Journal of the Electrochemical Society 1998;145:1374–81.
[20] Sun B, Rudkin R, Atkinson A. Effect of thermal cycling on residual stress and curvature of anode-supported SOFCs. Fuel Cells 2009;9(6):805–13.
[21] Liu X, Martin CL, Delette G, Bouvard D. Elasticity and strength of partially sintered ceramics. Journal of the Mechanics and Physics of Solids 2010;58(6):829–42.
[22] Anandakumar G, Li N, Verma A, Singh P, Kim JH. Thermal stress and probability of failure analyses of functionally graded solid oxide fuel cells. Journal of Power Sources 2010; 195(19):6659–70.
[23] Nakajo A, Van herle J, Favrat D. Sensitivity of stresses and failure mechanisms in SOFCs to the mechanical properties and geometry of the constitutive layers. Fuel Cells 2011;11(4): 537–52.
[24] Nakajo A. Thermomechanical and electrochemical in anode-supported solid oxide fuel cell stacks. Ph.D. thesis; 4930; Lausanne; 2011.
[25] Nakajo A, Kuebler J, Faes A,Vogt U, Schindler H, Chiang LK, et al. Compilation of mechanical properties for the structural analysis of solid oxide fuel cell stacks. Constitutive materials of anode supported cells. Ceramics International, in press.
[26] Liu W, Sun X, Stephens E, Khaleel M. Life prediction of coated and uncoated metallic interconnect for solid oxide fuel cell applications. Journal of Power Sources 2009;189(2): 1044–50.
[27] Nguyen B, Koeppel B, Ahzi S, Khaleel M, Prabhakar S. Crack growth in solid oxide fuel cell materials: from discrete to continuum damage modeling. J Am Ceram Soc 2006;89(4): 1358–68.
[28] Müller A, Becker W, Stolten D, Hohe J. A hybrid method to assess interface debonding by finite fracture mechanics. Engineering Fracture Mechanics 2006;73(8):994–1008.
[29] Gazzarri J, Kesler O. Short-stack modeling of degradation in solid oxide fuel cells: Part I. Contact degradation. Journal of Power Sources 2008;176(1):138–54.
[30] Stephens E, Vetrano J, Koeppel B, Chou Y, Sun X, Khaleel M. Experimental characterization of glass-ceramic seal properties and their constitutive implementation in solid oxide fuel cell stack models. Journal of Power Sources 2009; 193(2):625–31.
[31] Badiche X, Forest S, Guibert T, Bienvenu Y, Bartout JD, Ienny P, et al. Mechanical properties and non-homogeneous deformation of open-cell nickel foams: application of the mechanics of cellular solids and of porous materials. Materials Science and Engineering A 2000;289(1–2):276–88.
[32] Nakajo A, Wuillemin Z, Van herle J, Favrat D. Simulation of thermal stresses in anode-supported solid oxide fuel cell stacks. Part II: loss of gas-tightness, electrical contact and thermal buckling. Journal of Power Sources 2009;193(1): 216–26.
[33] Kawada T, Watanabe S, ichi Hashimoto S, Sakamoto T, Unemoto A, Kurumatani M, et al. Classification of mechanical failure in SOFC and strategy for evaluation of operational margin. ECS Transactions 2009;25(2):467–72.
[34] Larrain D, Van herle J, Maréchal F, Favrat D. Generalized model of planar SOFC repeat element for design optimization. Journal of Power Sources 2004;131(1–2): 304–12.
[35] Kim J, Liu W, Lee C. Multi-scale solid oxide fuel cell materials modeling. Computational Mechanics 2009;44(5):683–703.
[36] Lin CK, Chen TT, Chyou YP, Chiang LK. Thermal stress analysis of a planar SOFC stack. Journal of Power Sources 2007;164(1):238–51.
[37] Liu W, Sun X, Khaleel M. Effect of creep of ferritic interconnect on long-term performance of solid oxide fuel cell stacks. Fuel Cells 2010;10(4):703–17.
[38] Weil K, Koeppel B. Comparative finite element analysis of the stress-strain states in three different bonded solid oxide fuel cell seal designs. Journal of Power Sources 2008;180(1): 343–53.
[39] Weil K, Koeppel B. Thermal stress analysis of the planar SOFC bonded compliant seal design. International Journal of Hydrogen Energy 2008;33(14):3976–90.
[40] Govindaraju N, Liu W, Sun X, Singh P, Singh R. A modeling study on the thermomechanical behavior of glass-ceramic and self-healing glass seals at elevated temperatures. Journal of Power Sources 2009;190(2):476–84.
[41] Lin CK, Huang LH, Chiang LK, Chyou YP. Thermal stress analysis of planar solid oxide fuel cell stacks: effects of sealing design. Journal of Power Sources 2009;192(2): 515–24.
[42] Nakajo A, Wuillemin Z, Van herle J, Favrat D. Simulation of thermal stresses in anode-supported solid oxide fuel cell stacks. Part I: probability of failure of the cells. Journal of Power Sources 2009;193(1):203–15.
[43] Nakajo A, Mueller F, Brouwer J, Favrat D Van herle J, Favrat D. Progressive activation of degradation processes in SOFC stacks. Part I: lifetime extension by optimisation of the operating conditions, in press.
[44] Nakajo A, Mueller F, Brouwer J, Van herle J, Favrat D. Progressive activation of degradation processes in SOFC stacks. Part II: modelling of the spatial distribution of the degradation, in press.
[45] Nakajo A, Mueller F, McLarty D, Brouwer J, Van herle J, Favrat D. The effects of dynamic dispatch on the degradation of solid oxide fuel cell systems. The Journal of The Electrochemical Society 2011;158(11):B1329–40.

[46] Nakajo A, Mueller F, Brouwer J, Van herle J, Favrat D. Mechanical reliability and durability of SOFC stacks. Part I: modelling of the effect of the operating conditions on the reliability. International Journal of Hydrogen Energy 2012; 37(11):9249–68.
[47] Nakajo A, Tanasini P, Diethelm S, Van herle J, Favrat D. Electrochemical model of solid oxide fuel cell for simulation at the stack scale II: implementation of degradation processes. Journal of the Electrochemical Society 2011;158(9): B1102–18.
[48] Nakajo A, Wuillemin Z, Metzger P, Diethelm S, Schiller G, Van herle J, et al. Electrochemical model of solid oxide fuel cell for simulation at the stack scale I. Calibration procedure on experimental data. Journal of the Electrochemical Society 2011;158(9):B1083–101.
[49] gPROMS (General Process Modelling and Simulation Tool), v3.2, Process systems Enterprise Ltd, London.
[50] ABAQUS Inc., v6.8, Hibbitt, Karlsson and Sorensen, Rhode Island.
[51] Wuillemin Z. Experimental and modeling investigations on local performance and local degradation in solid oxide fuel cells. Ph.D. thesis; 4525; Lausanne; 2009.
[52] Metzger P, Friedrich KA, Müller-Steinhagen H, Schiller G. SOFC characteristics along the flow path. Solid State Ionics 2006;177(19–25):2045–51.
[53] Wuillemin Z, Nakajo A, Müller A, Schuler AJ, Diethelm S, Van herle J, et al. Locally-resolved study of degradation in a SOFC repeat-element. ECS Transactions 2009;25(2): 457–66.
[54] Jiang SP, Zhang JP, Apateanu L, Foger K. Deposition of chromium species at Sr-doped $LaMnO_3$ electrodes in solid oxide fuel cells. I. Mechanism and kinetics. Journal of the Electrochemical Society 2000;147(11):4013–22.
[55] Jiang SP, Zhang JP, Foger K. Deposition of chromium species at Sr-doped $LaMnO_3$ electrodes in solid oxide fuel cells II. Effect on O_2 reduction reaction. Journal of the Electrochemical Society 2000;147(9):3195–205.
[56] Jiang SP, Zhang JP, Foger K. Deposition of chromium species at sr-doped $LaMnO_3$ electrodes in solid oxide fuel cells: III. Effect of air flow. Journal of the Electrochemical Society 2001; 148(7):C447–55.
[57] Fergus JW. Effect of cathode and electrolyte transport properties on chromium poisoning in solid oxide fuel cells. International Journal of Hydrogen Energy 2007;32(16): 3664–71.
[58] Nielsen J, Hagen A, Liu Y. Effect of cathode gas humidification on performance and durability of solid oxide fuel cells. Solid State Ionics 2010;181(11–12):517–24.
[59] Kuhn B, Jimenez CA, Niewolak L, Huttel T, Beck T, Hattendorf H, et al. Effect of Laves phase strengthening on the mechanical properties of high Cr ferritic steels for solid oxide fuel cell interconnect application. Materials Science and Engineering A 2011;528(18):5888–99.
[60] Kleveland K, Orlovskaya N, Grande T, Moe AMM, Einarsrud MA, Breder K, et al. Ferroelastic behavior of $LaCoO_3$-based ceramics. Journal of the American Ceramic Society 2001;84(9):2029–33.
[61] Lein H, Andersen O, Vullum P, Lara-Curzio E, Holmestad R, Einarsrud MA, et al. Mechanical properties of mixed conducting $La_{0.5}Sr_{0.5}Fe_{1-x}Co_{1-x}O_{3-6}$ ($0 \leq x \leq 1$) materials. Journal of Solid State Electrochemistry 2006;10(8):635–42.
[62] MATLAB, v7.5, The Mathworks Inc., Natik.
[63] Mueller F, Jabbari F, Gaynor R, Brouwer J. Novel solid oxide fuel cell system controller for rapid load following. Journal of Power Sources 2007;172(1):308–23.
[64] Fardadi M, Mueller F, Jabbari F. Feedback control of solid oxide fuel cell spatial temperature variation. Journal of Power Sources 2010;195(13):4222–33.
[65] de Haart L, Mougin J, Posdziech O, Kiviaho J, Menzler N. Stack degradation in dependence of operation parameters; the real-SOFC sensitivity analysis. Fuel Cells 2009;9(6): 794–804.
[66] Delette G, Laurencin J, Dupeux M, Doyer J. Measurement of the fracture energy at the interface between porous cathode layer and electrolyte in planar solid oxide fuel cells. Scripta Materialia 2008;59(1):31–4.
[67] Lara-Curzio E, Wang Y, Shyam A, Trejo R, Armstrong B, Henry J, et al. Cathode-interconnect interfacial properties, http://www.netl.doe.gov/publications/proceedings/08/seca/Pres entations/3_ORNL_SECAWorkshop_Aug2008_final.pdf; 2008.
[68] Atkinson A, Selçuk A. Mechanical behaviour of ceramic oxygen ion-conducting membranes. Solid State Ionics 2000; 134(1–2):59–66.
[69] Gutierrez-Mora F, Ralph JM, Routbort JL. High-temperature mechanical properties of anode-supported bilayers. Solid State Ionics 2002;149(3–4):177–84.
[70] ThyssenKrupp. Material data sheet no. 4046. http://thyssenkruppvdm.de/_pdf/Crofer22APU_e.pdf.
[71] Haynes International. Material data sheet no. h-3000h. http://www.haynesintl.com/pdf/h3000.pdf.